AGU PUBLICATIONS

JGR

Journal of Geophysical Research: Oceans

RESEARCH ARTICLE

10.1002/2014JC010555

Modeled alongshore circulation and force balances onshore of a submarine canyon

Jeff E. Hansen[1,2], Britt Raubenheimer[2], Jeffrey H. List[3], and Steve Elgar[2]

[1]School of Earth and Environment, University of Western Australia, Crawley, Western Australia, Australia, [2]Woods Hole Oceanographic Institution, Woods Hole, Massachusetts, USA, [3]U. S. Geological Survey, Woods Hole, Massachusetts, USA

Key Points:
- A depth-averaged numerical model reproduced observed surfzone alongshore forcing
- The model indicates nonlinear advection plays an important role in the dynamics
- Residuals in field-based force balances may result from neglecting advection

Correspondence to:
J. E. Hansen,
jeff.hansen@uwa.edu.au

Citation:
Hansen, J. E., B. Raubenheimer, J. H. List, and S. Elgar (2015), Modeled alongshore circulation and force balances onshore of a submarine canyon, *J. Geophys. Res. Oceans*, *120*, doi:10.1002/2014JC010555.

Received 2 NOV 2014
Accepted 31 JAN 2015
Accepted article online 6 FEB 2015

Abstract Alongshore force balances, including the role of nonlinear advection, in the shoaling and surf zones onshore of a submarine canyon are investigated using a numerical modeling system (Delft3D/SWAN). The model is calibrated with waves and alongshore flows recorded over a period of 1.5 months at 26 sites along the 1.0, 2.5, and 5.0 m depth contours spanning about 2 km of coast. Field observation-based estimates of the alongshore pressure and radiation-stress gradients are reproduced well by the model. Model simulations suggest that the alongshore momentum balance is between the sum of the pressure and radiation-stress gradients and the sum of the nonlinear advective terms and bottom stress, with the remaining terms (e.g., wind stress and turbulent mixing) being negligible. The simulations also indicate that unexplained residuals in previous field-based estimates of the momentum balance may be owing to the neglect of the nonlinear advective terms, which are similar in magnitude to the sum of the forcing (pressure and radiations stress gradients) and to the bottom stress.

1. Introduction

Refraction of incident waves over shelf bathymetry, including canyons, deltas, and reefs, can result in a spatially variable wave field that can lead to alongshore variable surf zone forcing and circulation [*Long and Özkan-Haller*, 2005; *Thomson et al*., 2007; *Apotsos et al*., 2008; *Gorrell et al*., 2011; *Shi et al*., 2011]. As a result, bathymetric features well outside the surf zone can result in alongshore-variable surf zone forcing and flows, even along relatively uniform shorelines. The wave-averaged depth-integrated alongshore momentum balance in the surf zone can be given as [*Feddersen et al*., 1998]:

$$\rho(\eta+h)\left(\frac{\partial v}{\partial t}+u\frac{\partial v}{\partial x}+v\frac{\partial v}{\partial y}\right)=-\rho g(\eta+h)\frac{\partial \eta}{\partial y}-\frac{\partial S_{xy}}{\partial x}-\frac{\partial S_{yy}}{\partial y}-\tau_b+\tau_{wnd}-\nu\rho(\eta+h)\left(\frac{\partial^2 v}{\partial x^2}+\frac{\partial^2 v}{\partial y^2}\right) \quad (1)$$

where ρ is water density (assumed 1025 kg/m^3), η is the deviation of the mean water surface from the still water depth h, u and v are the depth and time-averaged current velocities in the cross shore (x) and alongshore (y) directions, respectively, and t is time. The left-hand side of the equation is the total acceleration $\left(\frac{Dv}{Dt}\right)$, which is the sum of local acceleration and the advective acceleration terms contributing to the alongshore balance. The acceleration is balanced by the alongshore pressure gradient $\left(\rho g(\eta+h)\frac{\partial \eta}{\partial y}\right)$, where g is the gravitational acceleration), the gradients of the diagonal and alongshore components of the radiation-stress tensor S_{xy} and S_{yy} [*Longuet-Higgins and Stewart*, 1964], the alongshore components of the bottom-stress and wind-stress vectors τ_b and τ_{wnd}, and the turbulent momentum flux owing to horizontal mixing $\nu\rho(\eta+h)\left(\frac{\partial^2 v}{\partial x^2}+\frac{\partial^2 v}{\partial y^2}\right)$, where ν is the horizontal eddy viscosity. For alongshore-uniform waves, alongshore flows are driven primarily by the radiation-stress forcing term $\left(\frac{\partial S_{xy}}{\partial x}\right)$ that results from the breaking-induced cross-shore dissipation of obliquely incident waves [*Longuet-Higgins*, 1970]. If an alongshore wave height gradient is present, a corresponding gradient in the wave setup (increase in mean sea level toward shore resulting from breaking waves [*Longuet-Higgins and Stewart*, 1964; *Lentz and Raubenheimer*, 1999; *Raubenheimer et al*., 2001]) is introduced, leading to an alongshore pressure gradient. Alongshore pressure gradients have been shown to drive alongshore flows at O(100 m) scales onshore of a submarine canyon [*Apotsos et al*., 2008; the same field site used here] and an ebb-tidal delta [*Shi et al*., 2011; *Hansen et al*., 2014]. Alongshore pressure gradients resulting from smaller-scale [O(10 m)] bathymetric features, such as a

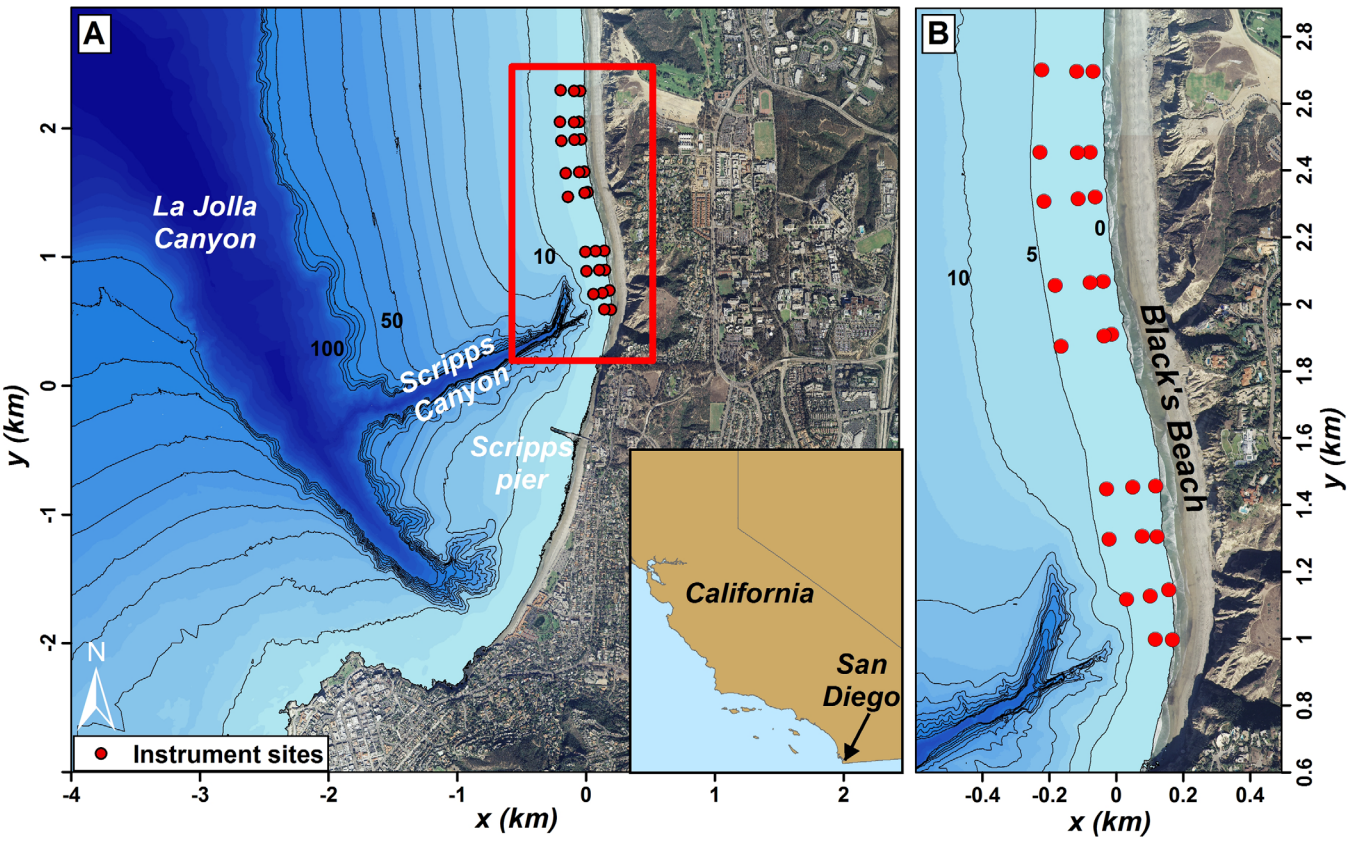

Figure 1. (a) Map showing La Jolla and Scripps submarine canyons (black curves are depth contours every 10 m to 100 m) near San Diego, CA (location shown in inset), as well as the study area (red box) and instrument sites (red circles). (b) Instrument sites (red circles) along the 1.0, 2.5, and 5.0 m depth contours (black curves). The local coordinate system is relative to the Scripps pier (visible in Figure 1a).

gap in a sand bar, also can be important for driving surf zone flows [*Putrevu et al.*, 1995; *Slinn et al.*, 2000; *Haller et al.*, 2002; *Chen et al.*, 2003; *Haas et al.*, 2003; *Schmidt et al.*, 2005]. Prior studies have suggested that the forcing of the alongshore currents by breaking obliquely incident waves and alongshore pressure gradients is balanced primarily by bottom stress [*Longuet-Higgins*, 1970; *Feddersen et al.*, 1998; *Feddersen and Guza*, 2003; *Apotsos et al.*, 2008]. However, modeling studies have suggested that nonlinear advection resulting from alongshore variations in forcing and bathymetry also may be a significant contribution to the momentum balance [*Long and Özkan-Haller*, 2005; *Kumar et al.* 2011, 2012; *Hansen et al.*, 2013; *Wilson et al.*, 2013].

The third-generation wave model Simulating WAves Nearshore (SWAN) has been used to model waves in coastal regions with gradual bathymetric variations [*Booij et al.*, 1999; *Ris et al.*, 1999; *Zubier et al.*, 2003], to examine the effects of offshore islands [*Rogers et al.*, 2007] on waves in intermediate depths, and to model the waves onshore of a steep submarine canyon [*Magne et al.*, 2007; *Gorrell et al.*, 2011]. Numerical wave-current coupled models based on the nonlinear shallow water equations have been used to simulate surf zone flows onshore of alongshore-variable bathymetry [*Long and Özkan-Haller*, 2005; *Benedet and List*, 2008; *Shi et al.*, 2011; *Hansen et al.*, 2013; *Wilson et al.*, 2013]. However, there have been few model-data comparisons of alongshore surf zone flows or momentum balances.

Here, alongshore flows and forcing from the shoreline to 6 m water depth onshore of a submarine canyon are investigated using a combination of observations and numerical model simulations (SWAN and Delft3D). In particular, model predictions of waves and flows and terms in the momentum balance are compared with observations. The model is used to examine the details of the alongshore force balance in areas that were not instrumented and to determine the contribution of terms neglected in field-based evaluations of the momentum balance.

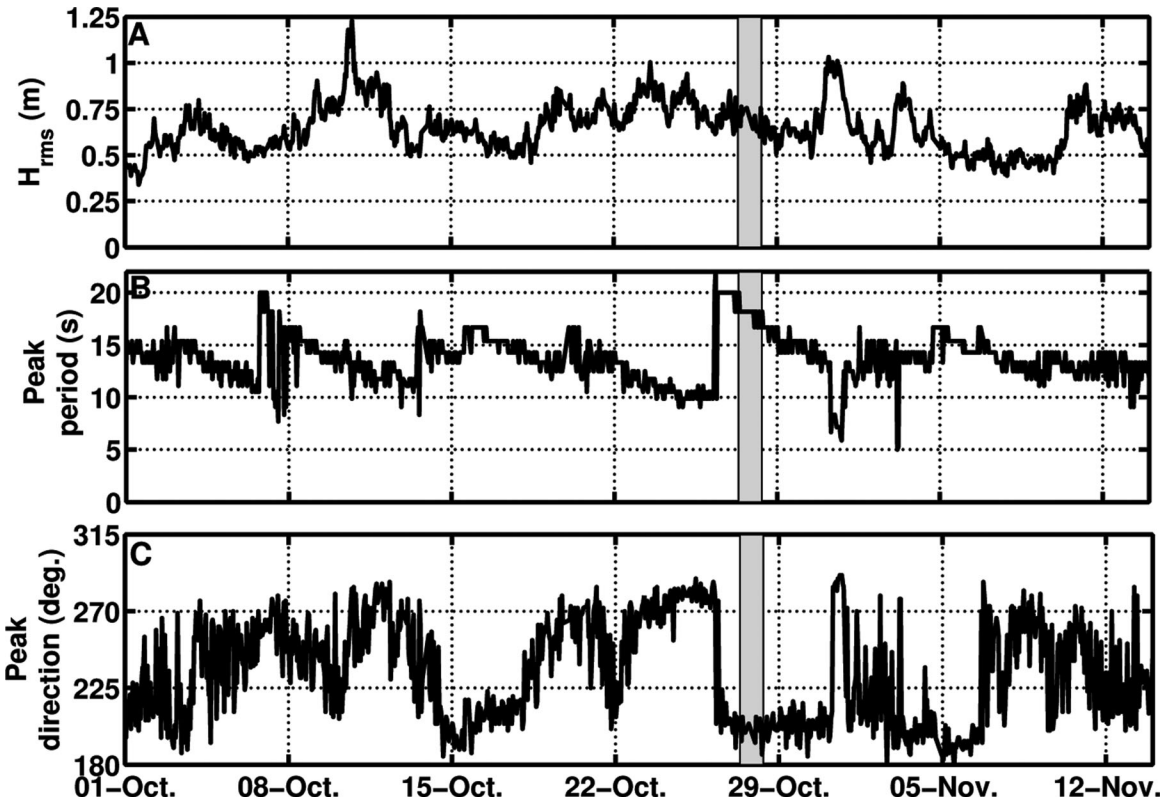

Figure 2. (a) Wave heights (H_{rms}), (b) peak period, and (c) peak direction observed at the CDIP Outer Torrey Pines buoy (depth ~ 550 m) versus date in 2003. The gray area indicates 27 October discussed in the text.

2. Observations

Observations were collected for 48 days in October and November 2003 at Black's Beach onshore of the Scripps submarine canyon near La Jolla, CA (Figure 1a). Colocated acoustic Doppler velocimeters (ADV) and pressure sensors were deployed at 26 sites along the 1.0, 2.5, and 5.0 m depth contours, forming nine cross-shore transects (Figure 1b) [*Apotsos et al.*, 2008]. The ADVs were sampled at 2 or 16 Hz for 3072 s (51.2 min) every hour. Sample volumes were located approximately 0.3, 0.3, and 0.9 m above sand level for sensors located in 1.0, 2.5, and 5.0 m depths, respectively. The pressure sensors were sampled at 2 Hz and were located approximately 0.5 m above the bed in 5.0 m depth and buried approximately 0.5 m below the bed in 1.0 and 2.5 m depth to avoid pressure disturbances owing to flow over the instrument [*Raubenheimer et al.*, 2001].

Bathymetry and topography were surveyed over the instrumented area approximately weekly. Bathymetry was surveyed to 6–8 m depth using a personal watercraft equipped with a single beam echo sounder and a Differential GPS (DGPS) system. Topographic surveys extending from the bluff base to the shoreline were conducted during low tide using a DGPS receiver mounted on an all-terrain vehicle or dolly. Both the bathymetric and topographic surveys consist of cross-shore transects with approximately 25–50 m alongshore spacing. Moreover, hourly estimates of the sand levels at the instrument locations in 1.0 and 2.5 m depth were obtained with the downward-looking ADVs. Additional bathymetry and topography were obtained from a U.S. Geological Survey seamless digital elevation model (DEM) compiled using several data sources, including LiDAR and multibeam bathymetry [*Barnard and Hoover*, 2010]. Bathymetry of the continental shelf (offshore of the DEM) is from NOAA National Ocean Service (NOS) surveys.

Water levels, water depths, wave frequencies, wave heights, and mean velocities were estimated for six 512 s (~8.5 min) periods each hour, and wave directions were estimated hourly [see *Apotsos et al.*, 2008]. Mean water levels were estimated assuming the pressure signal was hydrostatic. Setup was defined as the increase in the mean water level relative to that measured on the 3.5 m isobath at $y = 1300$ m (sensor not shown in Figure 1) [*Apotsos et al.*, 2008]. Mean water depths were estimated from the water levels and the

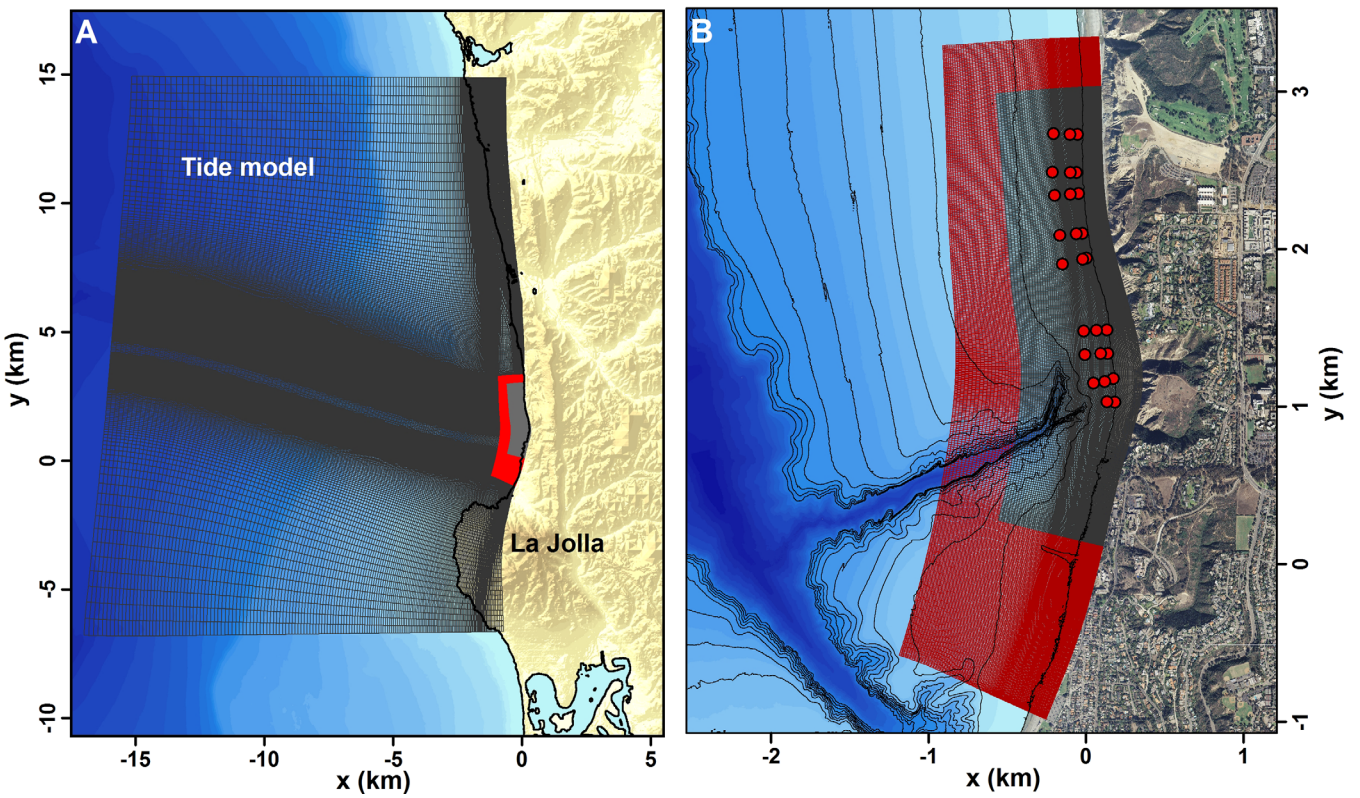

Figure 3. (a) Hydrodynamic domains used to reproduce the circulation. (b) Surf zone hydrodynamic domain (outer in red, inner in gray) with instrument sites indicated by red circles.

bathymetry (based on the surveys and the ADV measurements). Centroidal (energy weighted) incident wave frequencies and root mean square wave heights (H_{rms}) ($2\sqrt{2}$ times the standard deviation of the water surface fluctuations) were estimated from the pressure fluctuations between 0.05 and 0.30 Hz assuming linear wave theory and exponential decay of wave fluctuations through the bed [*Raubenheimer et al.*, 1998]. Mean wave angles were estimated using the colocated velocity and pressure observations [*Kuik et al.*, 1988; *Herbers and Guza*, 1990; *Herbers et al.*, 1999]. The diagonal component of the radiation-stress tensor (S_{xy}) was calculated at the 2.5 and 1.0 m depth sensors with linear wave theory using the estimates of wave height, direction, and frequency, and water depth [*Apotsos et al.*, 2008]. The alongshore component of the radiation-stress tensor (S_{yy}), as well as alongshore gradients ($\frac{\partial S_{yy}}{\partial y}$) were negligible relative to the remaining forcing terms, and thus are neglected.

Offshore wave conditions were obtained from the Coastal Data Information Program (CDIP) Outer Torrey Pines waverider buoy in 550 m water depth approximately 15 km NW of the experiment area. Frequency-directional (two-dimensional) wave spectra were estimated from the buoy observations every 30 min using the maximum entropy method [*Lygre and Krogstad*, 1986]. Wind speeds and directions were recorded by a meteorological station on the end of Scripps Pier at the southern end of the experiment area (Figure 1a). Offshore H_{rms} wave heights ranged from 0.3 to 1.3 m, peak periods ranged from 5 to 22 s, and peak incident wave directions (direction from) ranged from about 180° (south) to 290° (WNW) (Figure 2). Wind speeds ranged from calm to 16 m/s, but usually were light (mean 1.8 m/s). Maximum hourly averaged wave heights were 1.4 m at the 5 m depth sensors, and alongshore currents reached 0.8 m/s at the 1 m depth sensors. Tides were mixed semidiurnal with a maximum range of 2.1 m recorded at the NOAA Scripps Pier tide gauge.

3. Numerical Model

The observations from 1 October to 8 November were simulated with the numerical hydrodynamic model Delft3D [*Lesser et al.*, 2004, version 6.01.01.2703] coupled with the phase-averaged wave model SWAN [*Booij*

et al., 1999, version 40.72]. Delft3D solves the time-varying nonlinear shallow water equations on a staggered Arakawa-C grid using an alternating-direction-implicit solver [*Lesser et al*., 2004]. The circulation model consists of three domains: a large regional tide model (Figure 3a) forced with spatially variable, satellite-derived tidal constituents [*Egbert and Erofeeva*, 2002], and two higher-resolution curvilinear, shoreline-following "surf zone" domains (Figure 3b) that are two-way coupled and run simultaneously. The tide model is run without wave forcing and provides barotropic tidal forcing to the boundary of the outer surf zone domain via a combination of Neumann (depths $\lesssim$ 5 m) and Riemann (depths $\gtrsim$ 5 m) boundary conditions. In this application, these boundary conditions minimized boundary effects and allowed the nested surf zone domains to be smaller and more computationally efficient. Resolution of the surf zone domains in shallow water adjacent to the shoreline is $\sim$4 m in the cross shore and $\sim$8 m in the alongshore. Given the spatial resolution, a 1.5 s time step was used to minimize numerical error. The model was run in depth-averaged (2DH) mode to minimize run times. Although the vertical flow structure is not resolved, this approach reproduces the alongshore dynamics, which has weak vertical structure in shallow water [*Reniers et al*., 2004].

The bathymetry and topography data independently were organized into triangulated irregular networks that were used to interpolate elevation values onto the numerical domain nodes. In areas where multiple data sets overlapped, preference was given to the weekly surveys first and the NOS surveys last. Elevation data sets were merged smoothly when creating the bathymetry used in the model to avoid spurious flows resulting from artificial discontinuities in bed level. The bathymetry from the survey date closest to the time period of interest was used in the model.

The model bottom stress includes both a current-induced stress τ_c and a wave-generated stress τ_w, with both terms parameterized using quadratic drag laws [*Soulsby et al*., 1993],

$$\overrightarrow{\tau_c} = \frac{\rho g \overrightarrow{U} |\overrightarrow{U}|}{C_z^2}, \tag{2}$$

and

$$|\overrightarrow{\tau_w}| = \frac{1}{2} \rho f_w u_{orb}^2 \tag{3}$$

where $\overrightarrow{U}$ is the total Generalized Lagrangian Mean (GLM) velocity vector (the sum of time-averaged Eulerian and Stokes' drift components), f_w is a friction coefficient [$O(0.1)$] for oscillatory flow [*Swart*, 1974], and u_{orb} is the wave orbital velocity estimated from the wave height, frequency, and wavelength using linear theory. A spatially uniform Chezy (C_z) roughness of 70 $m^{0.5}/s$ (equivalent to a drag coefficient, C_d, of 0.002) was used in both the cross shore and alongshore directions in all hydrodynamic domains. The total bottom stress, τ_b, including current and wave components, is converted to an Eulerian reference frame by correcting for the Stokes' drift component of the GLM velocity. The total horizontal eddy viscosity (ν in equation (1)) in each grid cell is the sum of the background (ν_b) and turbulent (ν_t) components. The background horizontal eddy viscosity was calibrated to 0.5 m^2/s. The turbulent component (typically about 0.25–1.00 m^2/s) that results from wave breaking inside the surf zone is estimated as [*Battjes*, 1975]:

$$\nu_t = h_t \left(\frac{D_r}{\rho}\right)^{\frac{1}{3}}, \tag{4}$$

where D_r is the wave roller dissipation [*Nairn et al*., 1990; *Stive and de Vriend*, 1994; *Reniers and Battjes*, 1997] and h_t is the total water depth ($h+\eta$).

Wave propagation and evolution are simulated on three nested SWAN domains, with the largest extending seaward of the continental shelf break. The two largest domains are refined versions of those described previously [*Gorrell et al*., 2011], with the smallest domain the same as the combined surf zone hydrodynamic domains (Figure 3b). The largest wave domain is forced uniformly along the open boundaries with the 2-dimensional spectra derived from the offshore buoy observations. Winds were assumed to be spatially uniform, and white-capping dissipation was included [*van der Westhuysen et al*., 2007]. Although nonlinear triad interactions are not included, quadruplet interactions are. Within each domain, the spectral wave action balance [*Booij et al*., 1999] is solved using 88 directional bins ($\sim$3.5°/bin) and 37 frequency bins logarithmically

distributed between 0.03 and 1.00 Hz. The bottom friction coefficient associated with wave orbital motions was set to 0.038 m^2/s^3 in all SWAN domains [*Hasselmann et al*., 1973]. Stationary SWAN simulations were conducted every 20 min using updated water levels and flows from the hydrodynamic model.

Each stationary SWAN simulation provides the wave energy along the open boundary of the outer surf zone flow domain (Figure 3b, red region) and the mean wave direction and peak frequency at every grid cell within both surf zone domains (Figure 3b). The wave energy balance and radiation-stress gradients are computed using a "roller module" built into the hydrodynamic (flow) model. The roller module includes short-wave dissipation [*Roelvink*, 1993], using a calibrated breaker coefficient of $\gamma = 0.45$ (see Appendix A), as well as the roller energy balance and dissipation [*Reniers and Battjes*, 1997]. The advantage of using the roller module rather than using the spectral radiation-stress gradients directly from SWAN is the inclusion of the wave roller energy balance, which accounts for the cross-shore spatial lag between the wave breakpoint and the transfer of momentum to the water column. The resulting peak in alongshore flow is shoreward of the wave breakpoint, consistent with laboratory and field observations [*Reniers and Battjes*, 1997]. A second advantage of the roller module is the inclusion of enhanced eddy viscosity owing to wave breaking (equation (4)). The primary disadvantage of the roller module is that only a single frequency and direction are used to compute the radiation-stress gradients. For relatively narrow-banded frequency and directional spectra the use of a single frequency and direction is sufficient. In contrast, for bimodal spectra or in areas of strong refraction (e.g., landward of the canyon head), this assumption is not optimal [*Feddersen*, 2004], and likely contributes to model errors. However, the conclusions are insensitive to the method used to provide the radiation-stress gradients

Instantaneous output from the flow model, including water level (tide plus setup), depth-averaged velocity, and all terms of the cross shore and alongshore momentum equations at every grid cell, were saved every 10 min. For comparison with the observations, output from the grid cells closest to the instrument sites was extracted, and all vector quantities were rotated into the cross shore and alongshore coordinate system defined during the experiment (based on compass bearings at each transect). Model output and data sampling methods differ (instantaneous versus time-averaged). However, saving additional model output to enable averaging resulted in overly large files for each week run. Furthermore, wave forcing within the flow model is derived from stationary solutions to the phase-averaged action balance equation [*Booij et al*., 1999]. Model-data agreement was better when the model output and observations were averaged over 1 h periods than when the model output was interpolated to the 8.5 min times of the observational estimates. The model skill over the 1.5 month experiment is discussed in Appendix A.

4. Simulated Alongshore Momentum Balance

Analysis of the alongshore momentum balance is focused on 27 October 2003 (the case study described by *Apotsos et al*. [2008]) when near-temporally constant narrow-banded, low-frequency (18 s), ~0.75 m high waves approached the coast from the SSW (Figure 2). Results also are analyzed for 10 October 2003 (the case study examined by *Long and Özkan-Haller* [2005]) when a large rip current was simulated and observed visually at $y = 1600$ m. The alongshore variability of wave heights (Figures 4a–4c) and flows (Figure 4d) predicted on 27 October (Figure 4) and October 10 (not shown) are consistent with the observations (Figures 4c and 4d).

4.1. Model Validation With the Field-Estimated Momentum Balance

The model skill at reproducing the alongshore forcing is evaluated by comparing the pressure and radiation-stress gradients estimated from the model with those estimated from observations. The cross-shore gradient of S_{xy} was estimated as the gradient between the 2.5 and 1.0 m depth sensors, and the gradient between the 1.0 m depth sensor and the shoreline, where S_{xy} was assumed zero. These two gradients were averaged, producing an estimate at the "1.0 m depth" sensor. Curves of setup versus depth were generated for 24 h at each transect so that setup could be estimated along the bathymetric contour at the approximate depth of the "1.0 m depth" sensors [*Apotsos et al*., 2008]. Alongshore pressure gradients were estimated as the gradient between the adjacent upcoast and downcoast sites (central difference). Although the model outputs the computed momentum terms at each grid cell, the modeled forcing terms are calculated in the same manner as the field-based estimates (using the modeled water level and wave height, direction, and frequency interpolated to the 8.5 min averaging times of the observations) to ensure

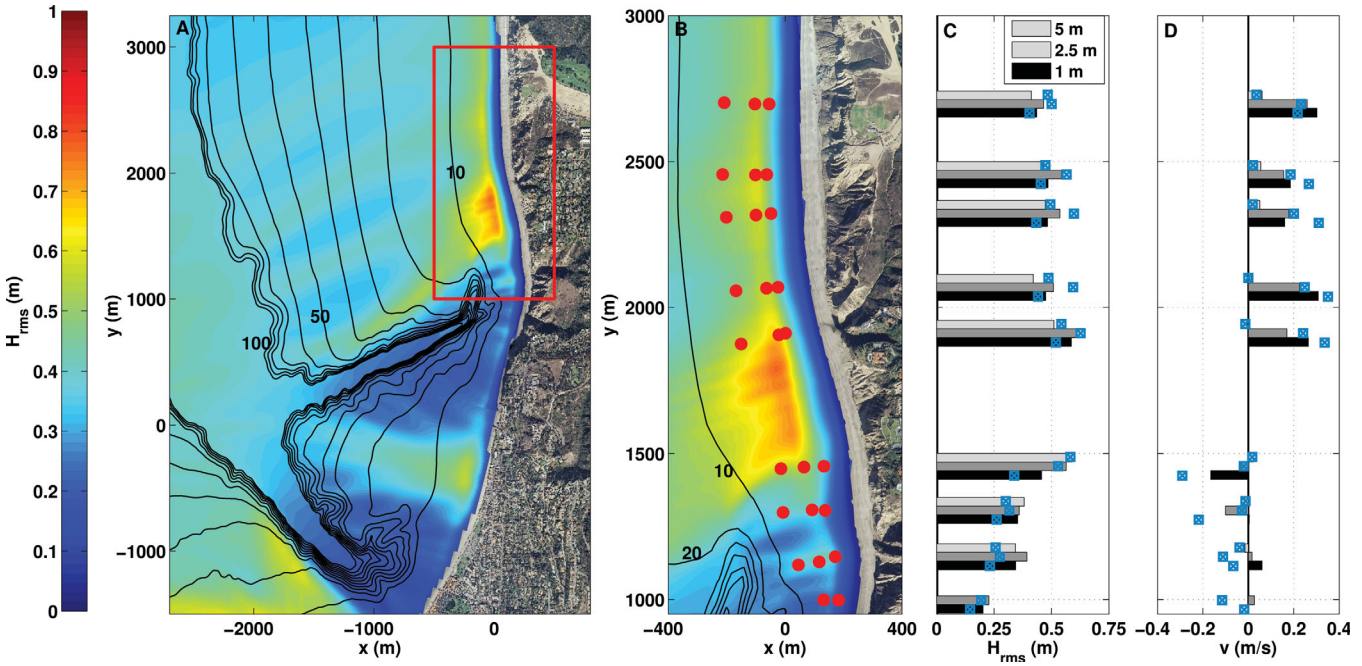

Figure 4. Regional (a) and experiment area (b, note different y scale) 24 h mean predicted wave heights (color contours, scale on left) and 24 h mean predicted (bars) and observed (blue squares) wave heights (c) and alongshore velocities (d) at the 26 instrument sites (red circles in Figure 4b) on 27 October 2003. Black curves in Figures 4a and 4b are depth contours every 10 m from 10 to 100 m, and the red rectangle in Figure 4a indicates the experiment area shown in Figure 4b.

comparisons of like quantities (e.g., pressure gradients were estimated using the water level difference between the sensor locations).

The modeled flows and forcing are overlaid on the field estimates (as presented in Figure 7 of *Apotsos et al.* [2008]) to examine the momentum balance (Figure 5, compare red with green symbols, and blue with orange symbols). Far from the canyon ($y = 2300$ m), the observed and predicted radiation-stress gradients were northerly directed (waves were from the south, positive gradient) and were larger than the opposing alongshore pressure gradients (Figure 5, compare red and green circles with squares), resulting in northerly directed alongshore flows (Figure 5, $y = 2300$ m velocities are positive). Closer to the canyon head ($y = 1450$ m), refraction of the incident waves over the canyon resulted in large alongshore wave height gradients and correspondingly large setup and pressure gradients toward the south (negative forcing in Figure 5) that were larger than the opposing radiation-stress gradients (Figure 5, compare blue and orange pluses with crosses), resulting in southerly directed alongshore flows (Figures 4d and 5, $y = 1450$ m velocities are negative). Near the canyon the model underestimates the observed alongshore pressure gradient by 10–20% (Figure 5, compare blue with orange crosses). Far from the canyon, the model reproduces the magnitude of the forcing, but underestimates the velocity (Figure 5, compare red with green symbols). Despite the errors between the observed and modeled alongshore forcing and velocity (see Appendix A), the model reproduces the relative importance of these terms at these locations (Figure 5), with pressure-gradient-dominated southerly flow near the canyon and radiation-stress-gradient-dominated northerly flow far from the canyon, suggesting the model can be used to examine the momentum balance further.

4.2. Modeled Momentum Balances

The model is used to investigate the alongshore force balance, retaining the terms previously assumed small, for the entire field site including the region with the largest alongshore variability ($1450 < y < 1900$ m) where instruments could not be deployed because of its popularity as a surfing location (spatial gap in the sensor array, Figure 1). The momentum terms from the 10 min instantaneous output were cross-shore integrated [*Hansen et al.*, 2013] from the shoreline to 6 m still water depth, then time averaged over 24 h on 27 October (gray region in Figure 2). The shoreline is defined as 0.25 m depth because the model does not resolve the physical processes in shallower depths owing to the grid resolution. The

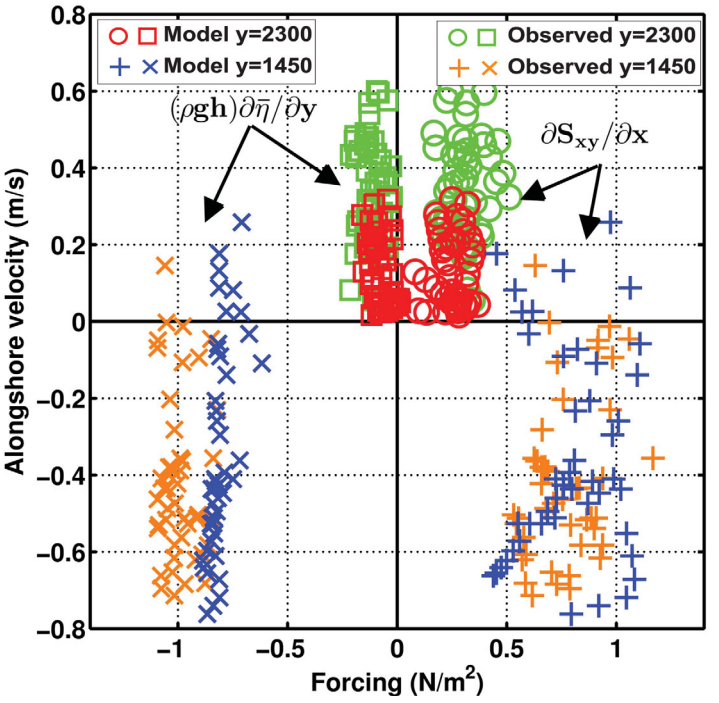

Figure 5. Observed (green $y=2300$ m and orange $y=1450$ m [from *Apotsos et al.*, 2008]) and modeled (red $y=2300$ m and blue $y=1450$ m) alongshore velocities versus radiation-stress (circles and pluses) and pressure gradients (squares and crosses) for 27 October (8.5 min data records). The sign of the forcing from equation (1) is retained when plotting (e.g., radiation-stress gradient is $-\frac{\partial S_{xy}}{\partial x}$) so that the term indicates the direction of forcing (positive is a force in the $+y$ direction).

offshore extent of the surf zone was chosen as 6 m depth, where the surf zone forcing decays to near zero. Results and conclusions do not change if the offshore integration depth is increased, but do change if the depth is decreased below ~5 m where surf zone flows are present. Although the computational domain is approximately shoreline following, all momentum terms were rotated into the local cross shore and alongshore coordinate system defined by the orientation of the 0.25 m depth contour. Results are not qualitatively dependent on the cross-shore integration, with the force balances along individual bathymetric contours similar to each other. However, the cross-shore integration reduces the importance of the horizontal mixing terms in (1), while providing a more representative estimate of surf zone forcing compared with estimates on individual depth contours. Wind stresses and $\frac{\partial S_{yy}}{\partial y}$ are small (and neglected in the discussion below). Thus, the dominant terms in the time-averaged cross-shore integrated momentum balance are the total acceleration, the alongshore-pressure gradient, the diagonal radiation-stress gradient, and the bottom stress.

Similar to previous results [*Apotsos et al.*, 2008], the modeled time-averaged cross-shore integrated alongshore force balance for 27 October (Figures 6b–6d) is spatially variable, with flows diverging at y ~ 1600 m (Figures 4d and 6a), consistent with the observations (Figure 4d). The model acceleration term (*Dv/Dt*), while small relative to the magnitudes of the pressure and radiation-stress gradients, is of the same magnitude as both the bottom stress (Figure 6b) and the sum of forcing by pressure and radiation-stress gradients (Figure 6d). Northward radiation-stress gradients dominate the forcing north of the canyon ($1600 \leq y \leq 2000$ m) and southward alongshore-pressure gradients dominate for $1400 \leq y \leq 1600$ m (Figure 6d). The strongest northward flows are at about $1800 \leq y \leq 2200$ m (consistent with the observations, Figure 4d), which is north of the maximum total forcing ($y = 1875$ m in Figure 6d). The model suggests this offset is owing primarily to the advective terms because the difference between the forcing and bottom stress is accounted for by acceleration (Figure 7a, compare black (forcing) and blue (bottom stress) curves with near perfect agreement between black and red-dashed (sum of bottom stress and acceleration) curves). For example, at $y \sim 2050$ m the flows remain about 0.5 m/s although the net forcing is decreasing (Figures 6a and 6d), consistent with a contribution of *Dv/Dt* to the force balance (Figure 7a). The strongest modeled southward flows are at $y \sim 1550$ m (Figure 6a), where the net southward forcing is largest (Figure 6d). The contribution to *Dv/Dt* of the local acceleration is small, whereas the contributions of the two advective terms are spatially variable, but of similar overall magnitudes (Figure 7b).

Field-based results for the 50 1 h periods that met the criteria of (1) having large wave height gradients near the canyon head and (2) the sensors along the 1.0 m isobaths were in the surf zone [from *Apotsos et al.*, 2008] suggest that the sum of the radiation-stress and pressure forcing is balanced by the quadratic bottom stress, estimated as $\rho\ v|\vec{U}|$ (computed using the ADV measured velocities) multiplied by a drag

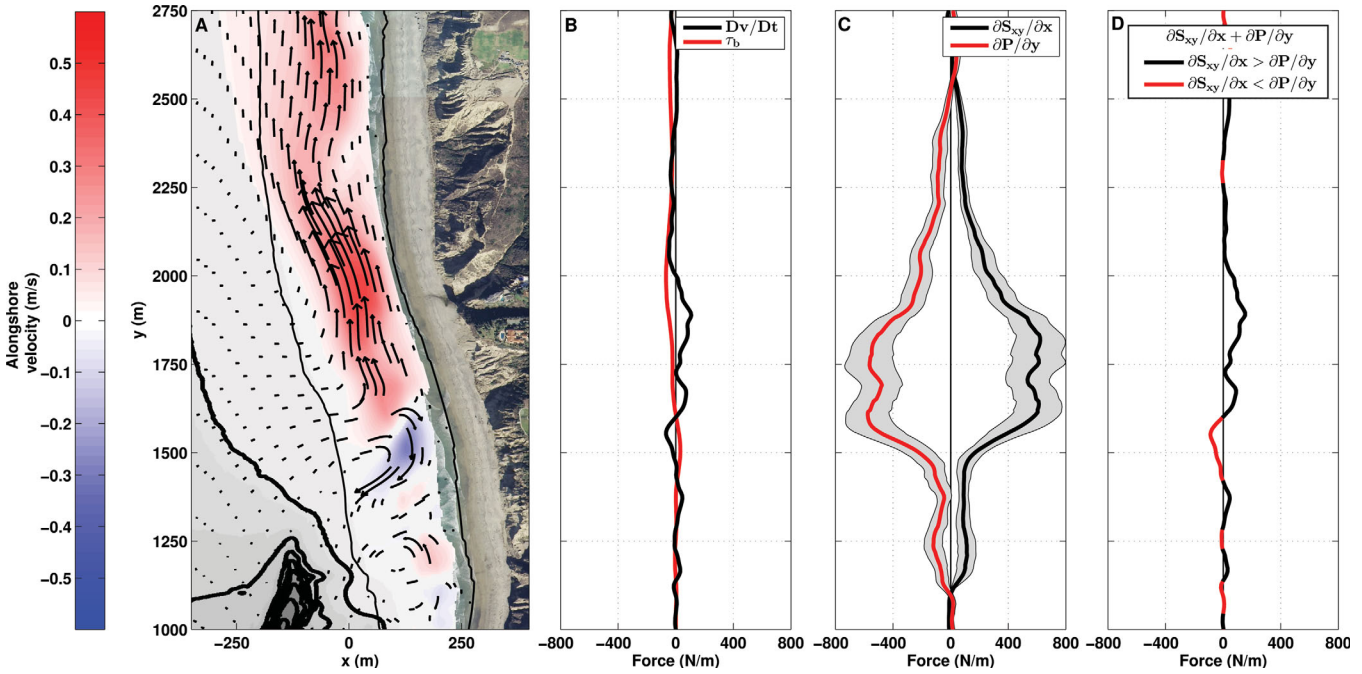

Figure 6. Modeled (a) 24 h mean alongshore velocity vectors for 27 October 2003 (colors indicate magnitude of the alongshore component (scale on left)). Alongshore structure of cross-shore integrated and 24 h averaged (B) *Dv/Dt* (black) and bottom stress (red), (c) radiation-stress (black) and pressure (red) gradients with gray bands indicating +/- one standard deviation over the 24 h period, and (d) sum of the pressure and radiation-stress gradients. In Figure 6d, the color indicates which forcing term is larger (black is radiation-stress > pressure gradient, red is pressure gradient > radiation-stress gradient).

coefficient estimated as the least-squares slope between the forcing and bottom stress (with R^2=0.71 and 0.75 near and far from the canyon, respectively). In contrast, the numerical model predicts that the bottom stress (see equations (2) and (3)) and total acceleration, which is dominated by the nonlinear advection ($v\frac{\partial v}{\partial y}$, $u\frac{\partial v}{\partial x}$, Figure 7b), are of similar magnitude (Figures 6b and 7a). The near perfect model agreement between the sum of the radiation-stress and pressure forcing terms and the sum of the total acceleration and bottom stress (Figure 7a, compare the black with the dashed red curve) indicates that the horizontal mixing and wind stress terms are negligible in the time-averaged cross-shore-integrated momentum balance.

The predicted force balance, and in particular the importance of the nonlinear advective terms, is similar for a range of wave conditions. For example, although the forcing terms were larger for the 1 m high, near-normally incident waves on 10 October (Figure 2, and the case study described in *Long and Özkan-Haller* [2005]), the simulated alongshore flows were similar in magnitude to those on 27 October, owing to a partial balance between the northward radiation-stress forcing and the southward pressure-gradient forcing (not shown). Similar to 27 October, the model suggests that both nonlinear advection and bottom stress are necessary to balance the net forcing. However, the locations of the flow convergences and divergences are dependent on the offshore wave conditions. For example, in contrast to 27 October, the simulated and observed 10 October alongshore flows converged north of the canyon head at $y \sim 1600$ m, and the model predicts offshore directed flows extending beyond the 10 m depth contour, similar to a rip-current. A strong rip current at roughly this location has been predicted previously [*Long and Özkan-Haller*, 2005] and is evident in images from 10 October (not shown).

5. Discussion

In the model, the sum of the pressure and radiations stress gradients (the forcing) is almost perfectly balanced (Figure 7a) by the sum of the bottom stress and total acceleration (which is dominated by nonlinear advection, Figure 7b). When nonlinear advection is neglected, the modeled forcing is correlated with a mean-current-induced bottom stress normalized by a drag coefficient (0.002) based on the Chezy

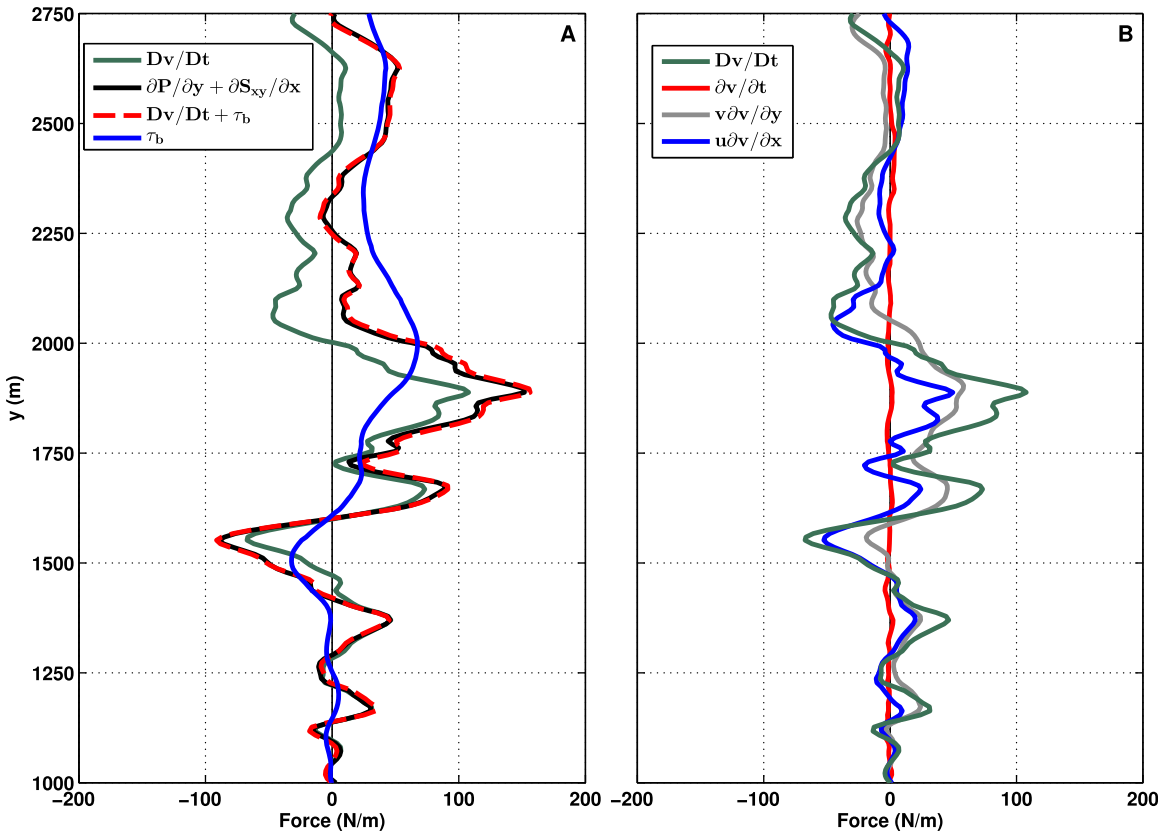

Figure 7. Modeled alongshore structure of (a) 24 h mean cross-shore integrated *Dv*/Dt (green curve), net forcing (sum of pressure and radiation-stress gradients, black curve), bottom stress (blue curve), and sum of bottom stress and *Dv/Dt* (dashed red curve), and (b) *Dv/Dt* (green curve), local acceleration (red curve) and nonlinear advection terms (gray and blue curves) for 27 October 2003. In Figure 7a, the bottom stress is moved to the left hand side of equation (1) for comparison with *Dv/Dt*.

roughness (equation (2)), but there is significant scatter (Figure 8a). The mean current-induced bottom stress roughly corresponds to the field-estimated stress $\rho v|\vec{U}|$, because the effects on the stress of the near normally incident waves (orthogonal to the mean current) are small [*Soulsby et al*., 1993]. North of the canyon at $y = 2300$ m, where the modeled *Dv/Dt* is small (Figure 7a), the least squares slope of the balance is 0.0026, similar to the model drag coefficient of 0.0020 and there is limited scatter (R^2=0.73, black circles in Figure 8a). Adjacent to the canyon at y=1450 m, where the model predicts large *Dv/Dt*, there is considerably more scatter ($R^2 = 0.26$, red squares in Figure 8a) and the least squares slope, 0.0035, is about 50% larger than the model drag coefficient. Including *Dv/Dt* in the balance removes nearly all scatter ($R^2 = 0.98$ and 0.89 for $y = 2300$ and 1450 m, respectively) and the drag coefficient (slope) is within 20% of that set in the model (Figure 8b). As suggested previously [*Apotsos et al*., 2008], these results indicate that neglecting nonlinear advection could be the cause of the scatter in field-based force balances. For example, the mean residuals from the least squares fits to the observations [*Apotsos et al*., 2008] were −0.54 and 0.35 N/m^2 for $y = 1450$ and 2300 m, respectively, similar to the model predicted *Dv/Dt* along the 1 m contour (approximate depth of field-estimated forcing). In addition, the quadratic dependence of both the bottom stress and advective terms suggests nonlinear advection could be accounted for in the field momentum balances by altering (increasing or decreasing, depending on the signs of the terms) the estimated bottom stress. Thus, neglecting the advective terms may have biased the field-estimated drag coefficients (0.0024 and 0.0025 at y=2300 and 1450 m, respectively) [*Apotsos et al*., 2008].

Similar to previous results [*Long and Özkan-Haller*, 2005], these new numerical results indicate that the acceleration term, principally nonlinear advection, can be as important as the sum of forcing (pressure and radiation-stress gradients) and as the bottom stress. Although the inclusion of nonlinear advection in the momentum balance does not change the underlying forcing (the direction of alongshore currents primarily is controlled by the sum of the pressure and radiation-stress gradients), the simulations suggest the

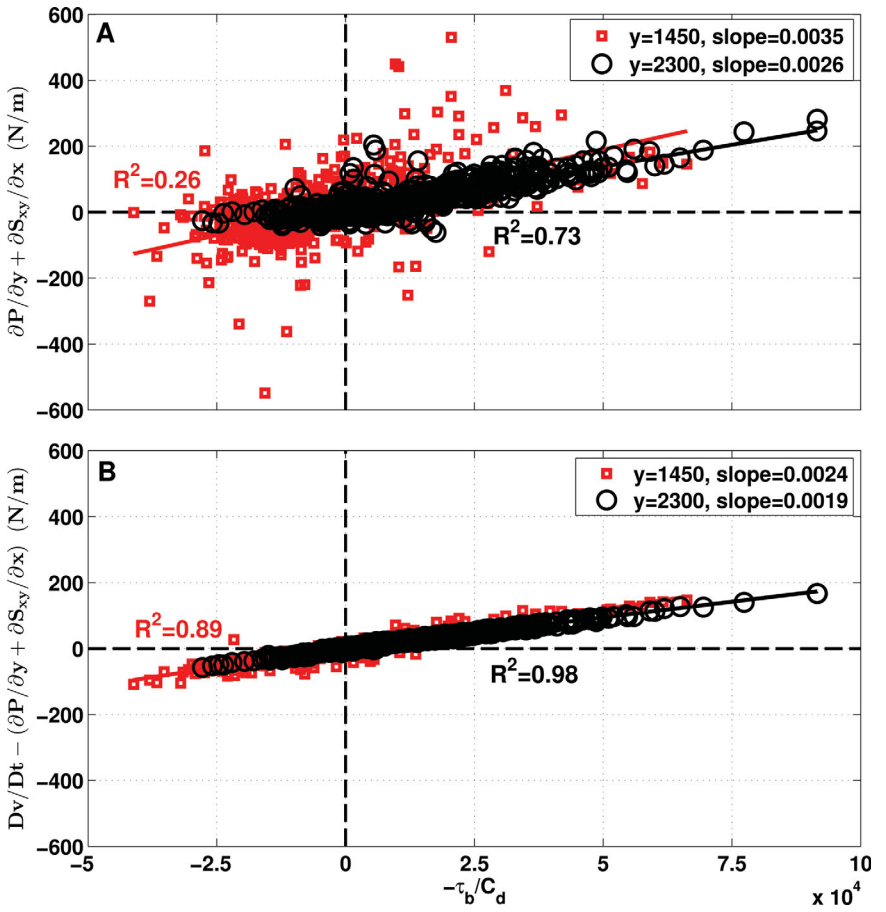

Figure 8. (a) Modeled cross-shore integrated net forcing (sum of pressure and radiation-stress gradients) versus bed stress term at y = 1450 (red squares) and 2300 m (black circles). (b) *Dv/Dt* minus net forcing versus bed stress term. Hourly averaged model results are shown for 35 days between 1 October and 7 November 2003. C_d within the model is set to 0.0020.

nonlinear advective terms are important to the spatial lags between the peaks in forcing and alongshore currents or bottom stresses, and alter the locations of flow convergences and divergences (Figures 6 and 7). Thus, nonlinear advection may be important to surf zone flow convergences (and rip locations) and morphologic change [*Wu and Liu*, 1984; *de Vriend*, 1987; *Long and Özkan-Haller*, 2005].

A scaling parameter, referred to as the shallow water Reynolds number (R_w) that approximates the alongshore length scales over which nonlinear advection likely is important is computed as [*Wilson et al.*, 2013]:

$$R_w = \frac{h_o v_o k}{\mu}, \tag{5}$$

where v_o represents the background, alongshore-independent, velocity in water depth h_o, $k = \frac{2\pi}{L}$, with L an alongshore length scale, and μ is a linear friction coefficient set to 0.002 m/s (following that used by *Wilson et al.* [2013]). The Reynolds number R_w is computed from the 24 h averaged numerical results on the 27 October along the 1 m still water depth contour (h_o =1 m) over length scales ranging from 50 to 500 m, with v_o given by the mean alongshore velocity magnitude over the respective alongshore length scale (Figure 9). Large R_w ($\gtrsim$ 10 for 0.5 m/s flows) occurs at short length scales where nonlinear advection acts to smooth alongshore variability in the flow [*Wilson et al.*, 2013]. Conversely, small R_w ($\lesssim$ 4) corresponds to long length scales for which the nonlinear advective terms can be neglected. Thus, although advection may be large locally, it may not be evident in field momentum balances [*Feddersen and Guza*, 2003; *Apotsos et al.*, 2008] owing to the large alongshore distances (i.e., small R_w) over which gradients were computed [*Wilson et al.*, 2013]. The numerical simulations indicate that the length scales for which R_w is small are as

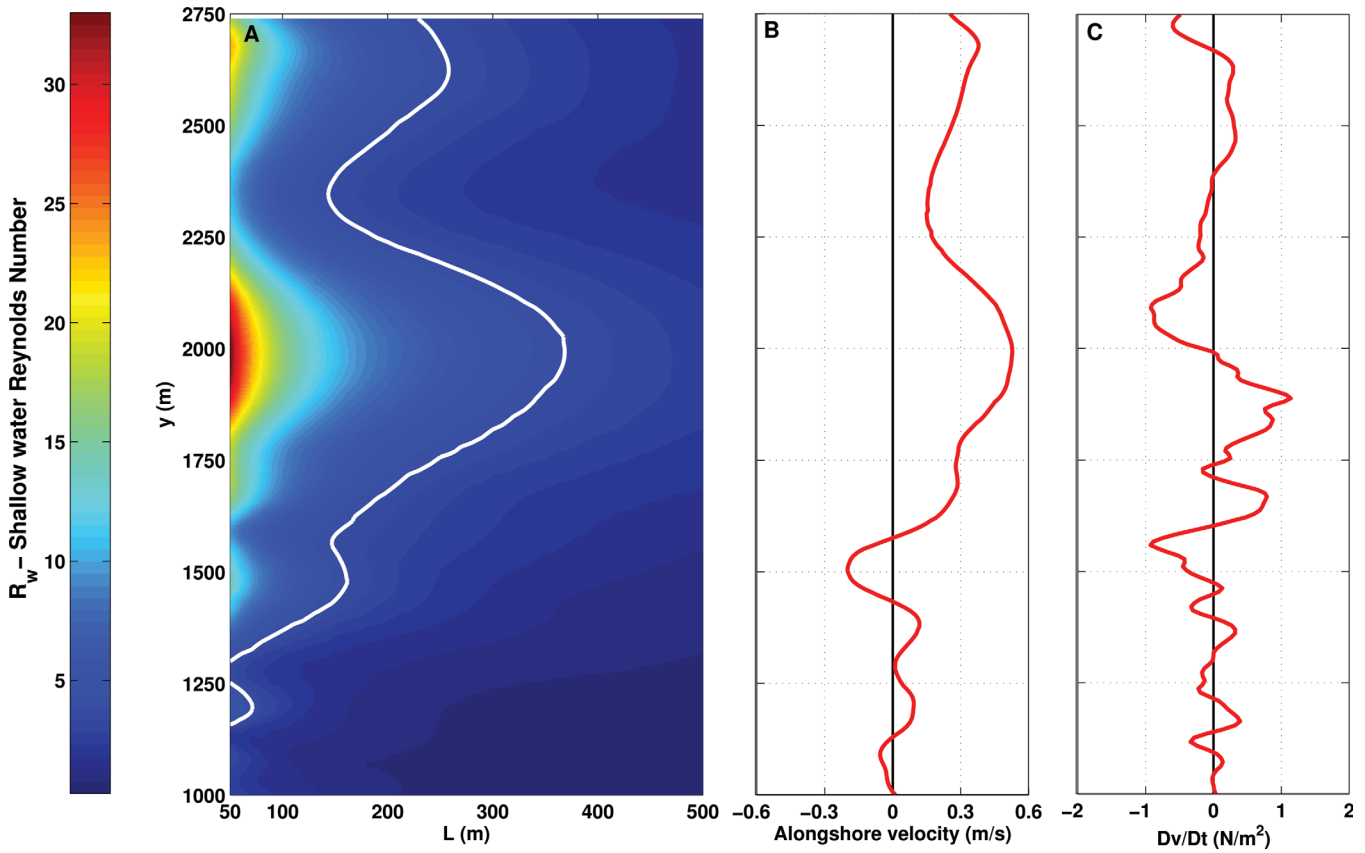

Figure 9. (a) Contours (scale on the left) of modeled 24 h R_w, the shallow water Reynolds number [*Wilson et al.*, 2013, equation (7)] on 27 October computed along the 1 m depth contour versus the alongshore length scale. (b) Time-averaged alongshore velocity and (c) *Dv/Dt* along the 1 m depth contour. The white contour in Figure 9a is $R_w = 3.9$, equivalent to a smoothing of 75% of the velocity variability that would be present in a model neglecting the nonlinear advective terms (for nominal 0.5 m/s/flows) [see *Wilson et al.*, 2013].

short as 50 m at the southern edge of the domain ($y < 1100$ m), but are greater than 400 m at $y = 2000$ m, corresponding to the strongest flows (Figure 9). These distances are mostly less than those used to estimate the field momentum balances. However, the numerical momentum balances presented here suggest the nonlinear advective terms are potentially important, but that their contribution is included in the parameterized drag coefficient and in the scatter (residuals) in the field-based momentum balances (Figure 8). Here, the length scales over which nonlinear advection is important appear to be determined primarily by the canyon-induced alongshore variability in the forcing (Figure 4), rather than by weakly varying inner surf zone bathymetry considered previously [*Wilson et al.*, 2013]. For example, between $y = 1250$ and 2000 m there are large alongshore gradients in the sum of the forcing (Figure 7) corresponding to the large gradients in the wave field (Figures 4b and 4c). In this region, *Dv/Dt* is large and fluctuates with the sum of the forcing at length scales ranging from ~100 to ~250 m.

6. Conclusions

Numerical simulations with a depth-averaged model (SWAN and Delft3D) reproduce the forcing and flows observed onshore of complex inner shelf bathymetry that includes a submarine canyon. Modeled momentum balances indicate the primary forcing, consisting of the sum of the pressure and radiation-stress gradients, is balanced by the sum of bottom stress and nonlinear advection. The simulations suggest that much of the scatter (residual) in a field-based balance between the total forcing and the bottom stress [*Apotsos et al.*, 2008] may be owing to the neglected nonlinear advective terms. In addition, neglecting nonlinear advection can lead to incorrect estimation of the drag coefficient by attributing advective effects to bottom stress. Although advection does not affect the direction of alongshore currents, it can affect the spatial patterns of the flow field.

Appendix A : Model Performance

Model-data comparisons were made for ~30 days using hourly averages calculated from six instantaneous model outputs saved every 10 min and from six 8.5 min means of the observations (~51 min). The root mean square error normalized by the variance of the observations (NRMSE), bias, and squared correlation coefficient (R^2) between the hour-averaged modeled and observed water depth, wave height, mean direction, radiation stress, and Eulerian alongshore flows were calculated at each of the 26 instrument sites (Figure A1). Note that the water depth and flow are output from the hydrodynamic model, the wave height is computed using the roller module (which includes short-wave dissipation and the wave roller energy balance) within the hydrodynamic model, the mean direction is calculated from the SWAN output used to drive the roller module, and the bulk radiation stress is calculated from the water depth, the root mean-squared wave height, mean direction, and peak period (output by SWAN). In addition, the Willmott Skill [*Willmott*, 1981] and Murphy Skill [*Murphy*, 1988] metrics, which were developed for comparing time series of model output with observations, were evaluated. Willmott Skill (*WS*) is computed as:

$$WS = 1 - \frac{\sum_{i=1}^{N} |X_{mod} - X_{obs}|^2}{\sum_{i=1}^{N} \left(|X_{mod} - \bar{X}_{obs}| + |X_{obs} - \bar{X}_{obs}| \right)^2}, \tag{A1}$$

where X_{mod} and X_{obs} are the modeled and observed variables of interest, respectively, and the overbars represent time averaging over the length of the time series with N samples (the mean N for all sites was 708 spanning about 30 days total including some data gaps). A skill of one indicates perfect agreement, whereas zero indicates "complete disagreement" [*Willmott*, 1981]. The Murphy Skill (*MS*) is:

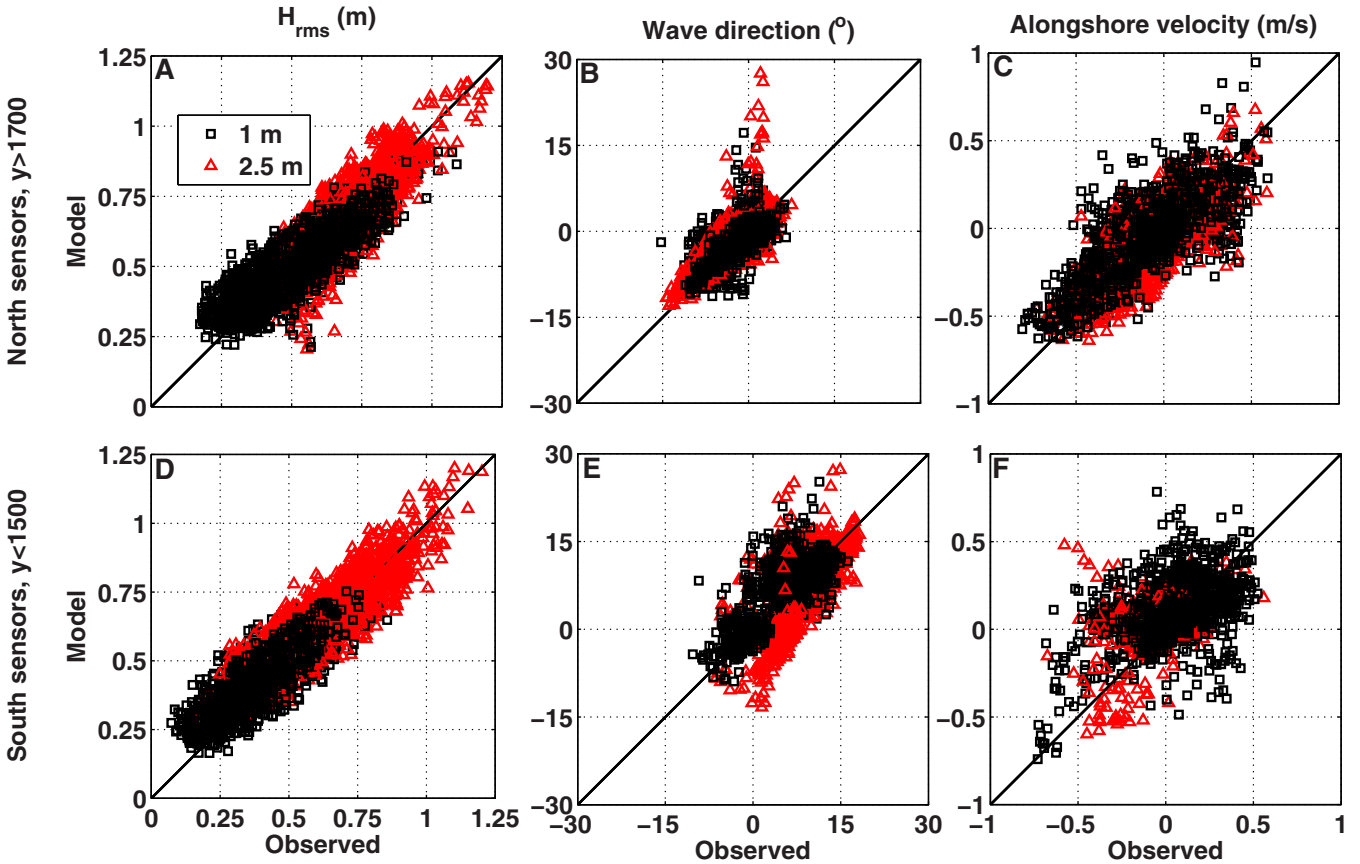

Figure A1. Model predictions versus observations of hourly averaged root mean square wave heights (a and d), mean wave directions (b and e), and alongshore velocities (c and f) at the 2.5 (red triangles) and 1.0 m (black squares) depth sensors north of $y = 1700$ (Figures A1a–A1c) and south of $y = 1500$ m (Figures A1d–A1f). Units are given in the plot titles.

Table A1. Variance Normalized Root Mean Square Error (*NRMSE*), Wilmott Skill (*WS*), Murphy Skill (*MS*), Bias, and Squared Correlation Coefficient (R^2) Between the Hourly Averaged Modeled and Observed Water Depth and Eulerian Alongshore Velocity for Approximately 30 days (Mean $N=708$, Depends on Availability of Instrument Data) at the 1.0, 2.5, and 5.0 m Depth Sites at Each Transect (Identified by Alongshore *y* Distance)

		Water Depth					Alongshore Velocity				
y (m)	Depth (m)	*NRMSE (-)*	*WS (-)*	*MS (-)*	Bias (m)	R^2 (-)	*NRMSE (-)*	*WS (-)*	*MS (-)*	Bias (m/s)	R^2 (-)
2700	1	0.14	0.94	0.78	−0.01	0.79	1.35	0.64	−1.06	0.09	0.17
	2.5	0.10	0.93	0.74	0.06	0.76	1.20	0.65	−0.66	0.05	0.20
	5	0.04	0.94	0.78	−0.05	0.80	1.15	0.36	−0.33	−0.02	0.01
2450	1	0.13	0.94	0.79	0.00	0.80	0.72	0.85	0.44	0.00	0.55
	2.5	0.09	0.95	0.80	0.00	0.81	0.70	0.84	0.46	−0.01	0.52
	5	0.04	0.94	0.77	−0.02	0.78	1.30	0.47	−0.71	0.00	0.01
2300	1	0.14	0.95	0.79	0.00	0.80	0.62	0.86	0.59	−0.04	0.59
	2.5	0.08	0.94	0.78	0.01	0.79	0.74	0.83	0.41	−0.01	0.48
	5	0.05	0.93	0.74	−0.03	0.75	1.22	0.53	−0.49	0.00	0.05
2060	1	0.14	0.94	0.78	0.00	0.79	0.72	0.83	0.41	−0.03	0.51
	2.5	0.10	0.94	0.79	0.02	0.80	0.80	0.83	0.32	0.01	0.50
	5	0.05	0.91	0.70	−0.02	0.71	1.13	0.51	−0.29	−0.01	0.07
1900	1	0.13	0.95	0.80	0.00	0.81	0.51	0.91	0.71	−0.03	0.72
	2.5	0.11	0.94	0.79	0.02	0.80	0.58	0.89	0.64	−0.02	0.65
	5	0.05	0.91	0.70	0.00	0.70	1.11	0.50	−0.23	−0.02	0.06
1450	1	0.15	0.94	0.77	0.01	0.78	0.86	0.70	0.22	−0.05	0.27
	2.5	0.08	0.95	0.81	0.02	0.82	1.21	0.59	−0.49	0.01	0.10
	5	0.04	0.94	0.77	−0.04	0.78	1.04	0.57	−0.09	−0.02	0.12
1300	1	0.15	0.95	0.79	0.02	0.80	1.15	0.63	−0.36	0.03	0.24
	2.5	0.10	0.95	0.80	0.01	0.81	0.93	0.59	−0.18	−0.01	0.12
	5	0.05	0.92	0.72	0.00	0.73	1.23	0.29	−0.56	−0.03	0.01
1130	1	0.17	0.93	0.75	−0.03	0.77	1.08	0.50	−0.21	−0.02	0.06
	2.5	0.08	0.94	0.77	−0.04	0.78	0.98	0.53	0.00	−0.03	0.11
	5	0.06	0.90	0.66	−0.02	0.67	1.23	0.45	−0.65	−0.01	0.02
1000	1	0.21	0.94	0.75	0.04	0.78	1.80	0.58	−3.13	0.14	0.30
	2.5	0.08	0.95	0.79	−0.06	0.81	1.27	0.39	−0.92	0.00	0.00

Table A2. Variance Normalized Root Mean Square Error (*NRMSE*), Wilmott Skill (*WS*), Murphy Skill (*MS*), Bias, and Squared Correlation Coefficient (R^2) Between the Hourly Averaged Modeled and Observed H_{rms}, Mean Wave Direction, and S_{xy} for Approximately 30 days (Mean $N=708$, Depends on Availability of Instrument Data) at the 1.0, 2.5, and 5.0m Depth Sites at Each Transect (Identified by Alongshore *y* Distance)

		H_{rms}					Wave Direction					S_{xy}				
y (m)	Depth (m)	*NRMSE (-)*	*WS (-)*	*MS (-)*	Bias (m)	R^2 (-)	*NRMSE (-)*	*WS (-)*	*MS (-)*	Bias (°)	R^2 (-)	*NRMSE (-)*	*WS (-)*	*MS (-)*	Bias (N/m)	R^2 (-)
2700	1	0.15	0.90	0.64	0.04	0.74	1.21	0.57	−1.18	−2.48	0.17	1.28	0.60	−1.01	−10.06	0.22
	2.5	0.10	0.94	0.76	0.01	0.81	1.03	0.74	−0.19	−0.33	0.35	1.06	0.74	−0.14	−3.36	0.32
	5	0.12	0.95	0.76	0.02	0.86	1.09	0.67	−0.76	−3.72	0.36	1.38	0.59	−1.25	−32.72	0.25
2450	1	0.13	0.91	0.70	0.00	0.70	0.96	0.56	−0.36	1.33	0.13	0.94	0.51	−0.19	8.75	0.10
	2.5	0.09	0.95	0.82	0.00	0.83	0.79	0.83	0.17	0.30	0.54	0.50	0.91	0.63	2.82	0.71
	5	0.26	0.85	0.42	0.09	0.67	1.07	0.46	−0.26	1.37	0.06	0.93	0.59	0.07	−4.29	0.14
2300	1	0.13	0.91	0.71	0.01	0.72	0.76	0.76	0.24	−0.30	0.35	0.86	0.61	0.04	0.70	0.16
	2.5	0.10	0.95	0.79	0.01	0.82	0.66	0.86	0.40	−0.31	0.58	0.40	0.94	0.77	−3.28	0.79
	5	0.12	0.95	0.77	0.03	0.87	0.95	0.51	−0.10	1.14	0.09	0.73	0.73	0.35	1.52	0.36
2060	1	0.15	0.90	0.67	0.03	0.71	0.68	0.77	0.10	1.13	0.39	0.61	0.83	0.39	5.86	0.51
	2.5	0.11	0.93	0.70	−0.02	0.76	0.59	0.82	0.29	0.80	0.50	0.45	0.89	0.63	8.36	0.68
	5	0.12	0.95	0.77	0.01	0.86	0.62	0.76	0.21	0.53	0.36	0.49	0.87	0.58	1.92	0.59
1900	1	0.15	0.86	0.59	−0.03	0.65	0.42	0.92	0.70	0.12	0.71	0.38	0.93	0.78	3.47	0.80
	2.5	0.11	0.90	0.60	−0.05	0.76	0.43	0.86	0.38	1.66	0.69	0.42	0.88	0.60	20.20	0.78
	5	0.13	0.94	0.71	0.01	0.82	1.38	0.58	−1.03	−7.96	0.40	1.53	0.60	−1.34	−63.63	0.39
1450	1	0.23	0.84	0.45	0.05	0.58	0.62	0.49	−0.78	2.01	0.05	0.90	0.49	−1.14	12.88	0.05
	2.5	0.11	0.95	0.79	−0.03	0.84	0.46	0.52	−0.38	0.89	0.05	0.35	0.88	0.65	−5.09	0.65
	5	0.12	0.95	0.77	−0.03	0.84	0.42	0.62	−0.62	−8.00	0.45	0.44	0.72	−0.29	−69.41	0.47
1300	1	0.19	0.90	0.67	0.04	0.79	0.46	0.60	−0.58	1.26	0.12	0.80	0.61	−0.87	10.18	0.17
	2.5	0.11	0.95	0.82	0.00	0.83	0.26	0.73	0.05	0.48	0.32	0.32	0.90	0.63	4.20	0.66
	5	0.16	0.95	0.79	0.05	0.85	0.33	0.69	−0.05	1.98	0.30	0.50	0.87	0.35	28.52	0.71
1130	1	0.20	0.90	0.63	0.05	0.77	0.79	0.73	0.07	−0.09	0.29	1.03	0.48	−0.28	−0.69	0.04
	2.5	0.17	0.93	0.76	0.05	0.84	1.20	0.39	−9.38	−5.82	0.30	1.09	0.44	−1.89	−38.97	0.03
	5	0.17	0.95	0.81	0.05	0.86	1.32	0.39	−0.88	2.96	0.04	1.62	0.23	−1.69	29.52	0.00
1000	1	0.21	0.90	0.67	0.00	0.68	2.37	0.34	−9.21	−3.15	0.04	2.03	0.27	−5.62	−6.98	0.01
	2.5	0.17	0.92	0.77	−0.02	0.81	1.24	0.44	−10.08	−2.93	0.31	0.94	0.52	−1.18	−12.21	0.17

$$MS = 1 - \frac{\sum_{i=1}^{N} (X_{mod} - X_{obs})^2}{\sum_{i=1}^{N} (X_{obs} - \bar{X}_{obs})^2}. \quad \text{(A2)}$$

An *MS* of one indicates perfect agreement, a zero indicates the model predictive ability is equivalent to using a mean of the observations, while an *MS* less than zero indicates the predictive ability is worse than using a mean of the observations. Further, (equation A2) can be shown to be equivalent to [*Murphy*, 1988; *Ralston et al*., 2010]:

$$MS = R^2 - \left(R - \frac{\sigma_{mod}}{\sigma_{obs}}\right)^2 - \left(\frac{\bar{X}_{mod} - \bar{X}_{obs}}{\sigma_{obs}}\right)^2, \quad \text{(A3)}$$

where σ indicates the standard deviation of the modeled (*mod*) or observed (*obs*) variable. In (equation A3) the first term is the squared correlation coefficient. The second term quantifies the ability of the model to reproduce the variance in the observations, and becomes zero if the least squares slope is one. The third term represents the disagreement of the model and observational means (bias) and corresponds to the linear regression intercept. Thus, the *MS* provides insight into the model performance. Although the *WS* commonly is used [*Li et al*., 2005; *Warner et al*., 2005; *Shi et al*., 2011; *Elias and Hansen*, 2013], it can produce skill scores of ~0.4 from a random uncorrelated time series [*Ralston et al*., 2010]. In the comparison that follows skill scores are termed "moderate" for $0.5 < WS < 0.75$ or $0.0 < MS < 0.5$, with "high" and "poor" skills for higher and lower scores.

Water depths, which are related primarily to tidal fluctuations, are reproduced well by the model with high skills (both *WS* and *MS*) and no consistent bias between sites (Table A1). The model simulates the wave heights with moderate to high skills at all sites (Table A2 and Figures A1a and A1d). The largest errors in wave direction and S_{xy} occur at $y = 1450$ and 1900 m, where alongshore variations in wave energy and incident directions are largest [*Gorrell et al*., 2011]. Although *WS* scores for directions and S_{xy} typically are "moderate", *MS* scores usually are "poor." Despite the sometimes-poor model skill, root mean square errors (not shown) and model bias for wave direction and S_{xy} usually are less than 5° and 50 N/m.

Alongshore flows in 1.0 and 2.5 m depth are reproduced well by the model for $1900 \leq y \leq 2450$ m with moderate to high skills (Table A1 and Figure A1c). Model skill is lower at the 5 m depth sites than at the shallower sites (Table A1) owing to a strong M_2 internal tide (which cannot be reproduced by the depth-averaged model) that resulted in observed flows as high as 0.30 m/s, particularly during spring tides [*Lentz et al*., 2004]. Harmonic analysis using *T_Tide* [*Pawlowicz et al*., 2002] of the observed flows at the 5 m depth sites attributes less than 0.1 m/s of the observed ~12 h variable alongshore velocities to the barotropic tidal band energy. This flow magnitude is consistent with the modeled flows.

The model tends to overestimate the alongshore flows at the sites immediately north of the canyon (Table A1 and Figure A1f, biases ~0.05–0.10 m/s for $1100 < y < 1500$ m), where the currents usually are weaker and more spatially variable than those far from the canyon ($y > 1500$ m). In addition, the model-data correlations are low near the canyon (Table A1, $y < 1500$ m). However, model alongshore flow root-mean-square errors are of similar magnitude at sites near ($y < 1500$ m) and far ($y > 1700$ m) from the canyon, but the weaker flows result in decreased model skill (compare Figures A1c with A1f, and Table A1).

The hourly averaged model results were most sensitive to the breaker coefficient (γ) and the background eddy viscosity (ν_b). The cross-shore wave height distribution was best reproduced with a $\gamma = 0.45$. However, the simulated wave heights were affected only slightly for $0.35 < \gamma < 0.50$, or for a γ that depends on depth and wave number [*Ruessink et al*., 2003]. The flow patterns were not sensitive to γ over this range, nor to the use of other dissipation formulations [*Battjes and Janssen*, 1978]. The spatial variability in the flows was best reproduced using a background eddy viscosity $\nu_b = 0.5$ m^2/s. However, the results were only weakly affected for $0.01 < \nu_b < 1.00$ m^2/s. Furthermore, cross-shore integrating the model results (as in Figures 6–8) reduces the sensitivity to horizontal mixing, and thus to the eddy viscosity.

Acknowledgments
The data used here are available at http://science.whoi.edu/users/elgar/NCEX/ncex.html. Funding was provided by a joint WHOI-USGS postdoctoral scholarship, NSF, ONR, and ASD(R&E). We thank Bob Guza and Tom Lippmann for helping to obtain the field observations and bathymetry, the PVLAB, and Scripps field crews for excellent logistical support, Alex Apotsos for providing field-based forcing estimates, and Pieter van der Linde and Levi Gorrell for providing their models of the area. Three anonymous reviewers are thanked for their comments and suggestions which improved the manuscript.

References

Apotsos, A., B. Raubenheimer, S. Elgar, and R. T. Guza (2008), Wave-driven setup and alongshore flows observed onshore of a submarine canyon, *J. Geophys. Res.*, *113*, C07025, doi:10.1029/2007JC004514.

Barnard, P. L., and D. J. Hoover (2010), A seamless, high-resolution coastal digital elevation model (DEM) for southern California, *U.S. Geol. Surv. Data Ser.*, 487, 8 p. [Available at http://pubs.usgs.gov/ds/487/.]
Battjes, J. A. (1975), Modelling of turbulence in the surf zone, paper presented at Symposium on Modeling Techniques, Am. Soc. Civ. Eng., San Francisco, Calif.
Battjes, J. A., and J. P. F. M. Janssen (1978), Energy loss and set-up due to breaking of random waves, paper presented at Proceedings of the 16th Conference on Coastal Engineering, Am. Soc. Civ. Eng., Hamb., Germany.
Benedet, L., and J. H. List (2008), Evaluation of the physical process controlling beach changes adjacent to nearshore dredge pits, *Coastal Eng.*, *55*, 1224–1236.
Booij, N., R. C. Ris, and L. H. Holthuijsen (1999), A third-generation wave model for coastal regions 1. Model description and validation, *J. Geophys. Res.*, *104*(C4), 7649–7666, doi:10.1029/98JC02622.
Chen, Q., J. T. Kirby, R. A. Dalrymple, F. Shi, and E. B. Thornton (2003), Boussinesq modeling of longshore currents, *J. Geophys. Res.*, *108*(C11), 3362, doi:10.1029/2002JC001308.
de Vriend, H. J. (1987), 2DH mathematical modelling of morphological evolutions in shallow water, *Coastal Eng.*, *11*(1), 1–27.
Egbert, G. D., and S. Y. Erofeeva (2002), Efficient Inverse modeling of barotropic ocean tides, *J. Atmos. Oceanic Technol.*, *19*(2), 183–204, doi: 10.1175/1520-0426(2002)019<0183:EIMOBO>2.0.CO;2.
Elias, E. P. L., and J. E. Hansen (2013), Understanding processes controlling sediment transports at the mouth of a highly energetic inlet system (San Francisco Bay, CA), *Mar. Geol.*, *345*, 207–220, doi:10.1016/j.margeo.2012.07.003.
Feddersen, F. (2004), Effect of wave directional spread on the radiation atress: Comparing theory and observations, *Coastal Eng.*, *51*, 473–481.
Feddersen, F., and R. T. Guza (2003), Observations of nearshore circulation: Alongshore uniformity, *J. Geophys. Res.*, *108*(C1), 3006, doi: 10.1029/2001JC001293.
Feddersen, F., R. T. Guza, S. Elgar, and T. H. C. Herbers (1998), Alongshore momentum balances in the nearshore, *J. Geophys. Res.*, *103*(C8), 15,667–615,676.
Gorrell, L., B. Raubenheimer, S. Elgar, and R. T. Guza (2011), SWAN predictions of waves observed in shallow water onshore of complex bathymetry, *Coastal Eng.*, *58*(6), 510–516, doi:10.1016/j.coastaleng.2011.01.013.
Haas, K., I. Svendsen, M. Haller, Q. Zhao (2003), Quasi-three-dimensional modeling of rip current systems, *J. Geophys. Res.*, *108*(C7), 3217,doi:10.1029/2002JC001355.
Haller, M. C., R. A. Dalrymple, and I. A. Svendsen (2002), Experimental study of nearshore dynamics on a barred beach with rip channels, *J. Geophys. Res.*, *107*(C6), 3061, doi:10.1029/2001JC000955.
Hansen, J. E., E. Elias, J. H. List, L. H. Erikson, and P. L. Barnard (2013), Tidally influenced alongshore circulation at an inlet-adjacent shoreline, *Cont. Shelf Res.*, *56*, 26–38, doi:10.1016/j.csr.2013.01.017.
Hansen, J. E., T. T. Janssen, B. Raubenheimer, F. Shi, P. L. Barnard, and I. S. Jones (2014), Observations of surf zone alongshore pressure gradients onshore of an ebb-tidal delta, *Coastal Eng.*, *91*(0), 251–260, doi:10.1016/j.coastaleng.2014.05.010.
Hasselmann, K., et al. (1973), Measurements of wind-wave growth and swell decay during the Joint North Sea Wave Project (JONSWAP), *Dtsch. Hydrogr. Z.*, *12*, Suppl.k A8, 12, 95 p.
Herbers, T. H. C., and R. T. Guza (1990), Estimation of directional wave spectra from multicomponent observations, *J. Phys. Oceanogr.*, *20*(11), 1703–1724, doi:10.1175/1520-0485(1990)020<1703:eodwsf>2.0.co;2.
Herbers, T. H. C., S. Elgar, and R. T. Guza (1999), Directional spreading of waves in the nearshore, *J. Geophys. Res.*, *104*(C4), 7683–7693, doi: 10.1029/1998jc900092.
Kuik, A. J., G. P. van Vledder, and L. H. Holthuijsen (1988), A method for the routine analysis of pitch-and-roll buoy wave data, *J. Phys. Oceanogr.*, *18*(7), 1020–1034, doi:10.1175/1520-0485(1988)018<1020:AMFTRA>2.0.CO;2.
Kumar, N., G. Voulgaris, and J. C. Warner (2011), Implementation and modification of a three-dimensional radiation stress formulation for surf zone and rip-current applications, *Coastal Eng.*, *58*(12), 1097–1117, doi:10.1016/j.coastaleng.2011.06.009.
Kumar, N., G. Voulgaris, J. C. Warner, and M. Olabarrieta (2012), Implementation of the vortex force formalism in the coupled ocean-atmosphere-wave-sediment transport (COAWST) modeling system for inner shelf and surf zone applications, *Ocean Modell.*, *47*, 65–95, doi:10.1016/j.ocemod.2012.01.003.
Lentz, S., and B. Raubenheimer (1999), Field observations of wave setup, *J. Geophys. Res.*, *104*(C11), 25,867–25,875, doi:10.1029/1999jc900239.
Lentz, S., T. H. C. Herbers, B. O'Reilly, P. Jessen, M. Kirk, S. Elgar, and R. T. Guza (2004), Observations of shoaling internal tidal waves during NCEX, *Eos Trans. AGU*, *85*(47), Fall Meet. Suppl., Abstract OS13C-03.
Lesser, G. R., J. A. Roelvink, J. A. T. M. van Kester, and G. S. Stelling (2004), Development and validation of a three-dimensional morphological model, *Coastal Eng.*, *51*(8-9), 883–915, doi:10.1016/j.coastaleng.2004.07.014.
Li, M., L. Zhong, and W. C. Boicourt (2005), Simulations of Chesapeake Bay estuary: Sensitivity to turbulence mixing parameterizations and comparison with observations, *J. Geophys. Res.*, *110*, C12004, doi:10.1029/2004JC002585.
Long, J. W., and H. T. Özkan-Haller (2005), Offshore controls on nearshore rip currents, *J. Geophys. Res.*, *110*, C12007, doi:10.1029/2005jc003018.
Longuet-Higgins, M. S. (1970), Longshore currents generated by obliquely incident sea waves 1, *J. Geophys. Res.*, *75*(33), 6790–6801, doi: 10.1029/JC075i033p06778.
Longuet-Higgins, M. S., and R. W. Stewart (1964), Radiation stresses in water waves: A physical discussion with application, *Deep Sea Res. Oceanogr. Abstr.*, *11*, 529–562.
Lygre, A., and H. E. Krogstad (1986), Maximum entropy estimation of the directional distribution in ocean wave spectra, *J. Phys. Oceanogr.*, *16*(12), 2052–2060, doi:10.1175/1520-0485(1986)016<2052:meeotd>2.0.co;2.
Magne, R., K. A. Belibassakis, T. H. C. Herbers, F. Ardhuin, W. C. O'Reilly, and V. Rey (2007), Evolution of surface gravity waves over a submarine canyon, *J. Geophys. Res.*, *112*, C01002, doi:10.1029/2005JC003035.
Murphy, A. H. (1988), Skill scores based on the mean square error and their relationships to the correlation coefficient, *Mon. Weather Rev.*, *116*(12), 2417–2424, doi:10.1175/1520-0493(1988)116<2417:ssbotm>2.0.co;2.
Nairn, R. B., J. A. Roelvink, and H. N. Southgate (1990), Transition zone width and implications for modelling surfzone hydrodynamics, in Coastal Engineering Conference, 1990: Proceedings of the International Conference, edited by B. L. Edge, pp. 68–81, Am. Soc. of Civ. Eng., Reston, Va.
Pawlowicz, R., B. Breardsley, and S. Lentz (2002), Classical tidal harmonic analysis including error estimates in MATLAB using T_TIDE, *Comput. Geosci.*, *28*(8), 929–937.

Putrevu, U., J. Oltman-Shay, and I. A. Svendsen (1995), Effect of alongshore nonuniformities on longshore current predictions, *J. Geophys. Res.*, *100*(C8), 16,119–16,130, doi:10.1029/95JC01459.
Ralston, D. K., W. R. Geyer, and J. A. Lerczak (2010), Structure, variability, and salt flux in a strongly forced salt wedge estuary, *J. Geophys. Res.*, *115*, C06005, doi:10.1029/2009JC005806.
Raubenheimer, B., S. Elgar, and R. T. Guza (1998), Estimating wave heights from pressure measured in sand bed, *J. Waterw. Port Coastal Ocean Eng.*, *124*(3), 151–154, doi:10.1061/(asce)0733-950x(1998)124:3(151).
Raubenheimer, B., R. T. Guza, and S. Elgar (2001), Field observations of wave-driven setdown and setup, *J. Geophys. Res.*, *106*(C3), 4629–4638, doi:10.1029/2000jc000572.
Reniers, A. J. H. M., and J. A. Battjes (1997), A laboratory study of longshore currents over barred and non-barred beaches, *Coastal Eng.*, *30*(1–2), 1–21, doi:10.1016/S0378-3839(96)00033-6.
Reniers, A. J. H. M., E. B. Thornton, T. P. Stanton, and J. A. Roelvink (2004), Vertical flow structure during Sandy Duck: Observations and modeling, *Coastal Eng.*, *51*(3), 237–260, doi:10.1016/j.coastaleng.2004.02.001.
Ris, R. C., L. H. Holthuijsen, and N. Booij (1999), A third-generation wave model for coastal regions 2. Verification, *J. Geophys. Res.*, *104*(C4), 7667–7681, doi:10.1029/1998JC900123.
Roelvink, J. A. (1993), Dissipation in random wave groups incident on a beach, *Coastal Eng.*, *19*(1–2), 127–150, doi:10.1016/0378-3839(93)90021-y.
Rogers, E. W., J. M. Kaihatu, L. Hsu, R. E. Jensen, J. D. Dykes, and K. T. Holland (2007), Forecasting and hindcasting waves with the SWAN model in the Southern California Bight, *Coastal Eng.*, *54*, 1–15, doi:10.1016/j.coastalend.2006.06.011.
Ruessink, B. G., D. J. R. Walstra, and H. N. Southgate (2003), Calibration and verification of a parametric wave model on barred beaches, *Coastal Eng.*, *48*(3), 139–149, doi:10.1016/s0378-3839(03)00023-1.
Schmidt, W. E., R. T. Guza, and D. N. Slinn (2005), Surf zone currents over irregular bathymetry: Drifter observations and numerical simulations, *J. Geophys. Res.*, *110*, C12015, doi:10.1029/2004JC002421.
Shi, F., D. M. Hanes, J. T. Kirby, L. Erikson, P. Barnard, and J. Eshleman (2011), Pressure-gradient-driven nearshore circulation on a beach influenced by a large inlet-tidal shoal system, *J. Geophys. Res.*, *116*, C04020, doi:10.1029/2010JC006788.
Slinn, D. N., J. S. Allen, and R. A. Holman (2000), Alongshore currents over variable beach topography, *J. Geophys. Res.*, *105*(C7), 16,971–16,998, doi:10.1029/2000jc900051.
Soulsby, R. L., L. Hamm, G. Klopman, D. Myrhaug, R. R. Simons, and G. P. Thomas (1993), Wave-current interaction within and outside the bottom boundary layer, *Coastal Eng.*, *21*(1–3), 41–69, doi:10.1016/0378–3839(93)90045-A.
Stive, M. J. F., and H. J. de Vriend (1994), Shear stresses and mean flow in shoaling and breaking waves, in Proceedings of the Twenty-Fourth International Conference, edited by B. L. Edge, pp. 594–608, Am. Soc. of Civ. Eng., Reston, Va.
Swart, D. H. (1974), Offshore sediment transport and equilibrium beach profiles, PhD thesis, Delft Univ. of Technology, Delft, Netherlands.
Thomson, J., S. Elgar, T. H. C. Herbers, B. Raubenheimer, and R. T. Guza (2007), Refraction and reflection of infra gravity waves near submarine canyons, *J. Geophys. Res.*, *112*, C10009, doi:10.1029/2007JC004227.
van der Westhuysen, A. J., M. Zijlema, and J. A. Battjes (2007), Nonlinear saturation-based whitecapping dissipation in SWAN for deep and shallow water, *Coastal Eng.*, *54*(2), 151–170, doi:10.1016/j.coastaleng.2006.08.006.
Warner, J. C., W. R. Geyer, and J. A. Lerczak (2005), Numerical modeling of an estuary: A comprehensive skill assessment, *J. Geophys. Res.*, *110*, C05001, doi:10.1029/2004JC002691.
Willmott, C. J. (1981), On the validation of models, *Phys. Geogr.*, *2*, 184–194.
Wilson, G. W., H. T. Özkan-Haller, and R. A. Holman (2013), Quantifying the length-scale dependence of surf zone advection, *J. Geophys. Res. Oceans*, *118*, 2393–2407, doi:10.1002/jgrc.20190.
Wu, C. S., and P. L. Liu (1984), Effects of nonlinear inertial forces on Nearshore currents, *Coastal Eng.*, *8*, 15–32.
Zubier, K., V. Panchang, and Z. Demirbilek (2003), Simulation of waves at Duck (North Carolina) using two numerical models, *Coastal Eng. J.*, *45*(03), 439–469, doi:10.1142/S0578563403000853.